Annals of Glaciology

Article

Cite this article: González-Santacruz N, Muñoz-Marzagon P, Bartolomé M, Moreno A, Huidobro J, Faria SH (2023). Effects of impurities on the ice microstructure of Monte Perdido Glacier, Central Pyrenees, NE Spain. *Annals of Glaciology* 1–14. https://doi.org/10.1017/aog.2023.66

Received: 31 December 2022
Revised: 7 September 2023
Accepted: 18 September 2023

Keywords:
glacial rheology; glacial sedimentology; ice core; ice dynamics; snow chemistry

Corresponding author:
Nicolás González-Santacruz;
Email: nagonzalez002@ikasle.ehu.eus

cambridge.org/aog

Effects of impurities on the ice microstructure of Monte Perdido Glacier, Central Pyrenees, NE Spain

Nicolás González-Santacruz[1,2], Patricia Muñoz-Marzagon[2], Miguel Bartolomé[3,4,5], Ana Moreno[6], Jennifer Huidobro[7] and Sérgio Henrique Faria[2,8]

[1]Department of Geology, University of the Basque Country (UPV/EHU), Leioa, Spain; [2]Basque Centre for Climate Change (BC3), Leioa, Spain; [3]Department of Geology, National Museum of Natural Sciences (CSIC), Madrid, Spain; [4]Swiss Institute for Speleology and Karst Studies (SISKA), La Chaux-de-Fonds, Switzerland; [5]Department of Earth Sciences, Geological Institute, Zurich, Switzerland; [6]Department of Geoenvironmental Processes and Global Change, Pyrenean Institute of Ecology (CSIC), Zaragoza, Spain; [7]Department of Analytical Chemistry, University of the Basque Country (UPV/EHU), Leioa, Spain and [8]IKERBASQUE, Basque Foundation for Science, Bilbao, Spain

Abstract

Monte Perdido Glacier, located in the central Pyrenees, is one of the southernmost glaciers in Europe. Due to climate change, this glacier is suffering an accelerated mass loss, especially in the last decades. If the current trends persist, this glacier is expected to disappear in the next 50 years. As part of the efforts of the scientific community to increase the knowledge about this glacier, this research presents the first microstructural characterization of the Monte Perdido Glacier, focused on a high-impurity concentration segment that belongs to an ice core drilled in 2017. The results reveal the ice has a layering defined by air bubbles and non-soluble impurities. The bubble-defined layering exhibits features of both a primary (sedimentary) and a secondary (strain-induced) origin. We found a clear inverse correspondence between the particle concentration and the grains' size and roundness index. A preliminary micro-Raman characterization of the particles shows the occurrence of atacamite, anatase (likely related to ancient mining activities in the vicinity of the glacier) and quartz. The latter could be an indicator of mineral dust, probably suggesting the arrival of dust-laden air masses from the north of the African continent.

Introduction

Global warming affects the cryosphere, increasing the flow and melt rates of large ice masses, thus accelerating sea level rise. A better understanding of ice mechanics is essential for improving projections of ice loss under various climate-change scenarios and refining ice dynamics models used for dating paleoclimate ice-core records (IPCC, 2021). The foundations of ice mechanics have been investigated through laboratory-based tests (e.g., Glen, 1955; Jacka and Maccagnan, 1984; Budd and Jacka, 1989; Treverrow and others, 2012). Experience suggests that polycrystalline isotropic ice flow follows a power law known in glaciology as *Glen's Flow law:*

$$\dot{\varepsilon} = A\sigma^n$$

where $\dot{\varepsilon}$ is the secondary (minimum) strain rate, A the flow parameter, σ the stress and the power exponent usually set to $n = 3$ (Glen, 1952, 1955). The flow parameter (A) is dependent on ice temperature, impurities and other factors (Kostecka and Whillans, 1988; Reeh, 1988; Dahl-Jensen, 1989; Cuffey and Paterson, 2010). The nature of the impurities is diverse, ranging from volcanic ash and sea salt to mineral dust and other aerosols (generated e.g. by forest fires or human activities). Once these aerosols are deposited over the snow surface, they become part of the ice in the form of dissolved or undissolved impurities (particles). The scientific literature refers to high-impurity layers as *cloudy bands (CB)* due to their turbid and darker appearance compared to the surrounding ice (e.g. Gow and Williamson, 1976; Faria and others, 2014). Impurities affect the ice flow through their interactions with the ice microstructure, including its grain sizes and shapes (grain stereology; Faria and others, 2018), and the fabric (preferential orientations of the *c*-axes). Ice cores extracted from polar areas (Siberia, Alaska, Northern Canada, Antarctica, Greenland) revealed a sharp decrease in the grain size inside the CB and a higher amount of this type of layers in glacial periods (Paterson, 1991; Thorsteinsson and others, 1995; Faria and others, 2014). For instance, that effect is noticeable in ice belonging to the transition between the Holocene and the Last Glacial Maximum (Duval and Lorius, 1980; Petit and others, 1987; Lipenkov and others, 1989; Thorsteinson and others, 1997).

Some of the early works linking the debris-rich levels to changes in ice rheology were Swinzow (1962), Gundestrup and Hansen (1984), Etheridge (1989) or Paterson (1991). For example, one of the analyses consisted of monitoring a borehole closure rate in the Devon Island ice cap (Canadian Arctic), where results revealed an anomalous closure rate near the

https://doi.org/10.1017/aog.2023.66 Published online by Cambridge University Press

bottom. Subsequent dating showed the ice with this peculiar mechanical behaviour belonged to the Last Glacial Cycle (~115–11.5 ka; Dansgaard, 1973). Later, Fisher and Koerner (1986) observed the same phenomena in the Agassiz ice cap. Paterson (1991) found that, for a given temperature and shear stress value, the ice strain rate of the Last Glacial Maximum ice was three times higher than the Holocene ice. Furthermore, it was observed that the crystallographic *c*-axes tended to approach a vertical maximum (Paterson, 1991) due to the rotation of grains under a simple shear regime, forcing the basal planes (where preferential slip occurs) to lie parallel to the shear plane, creating a favourable condition for ice deformation and flow. That maximum will be more marked compared to other fabrics where the *c*-axes exhibit similar arrangements, such as those caused by uniaxial compression, in which they are around the vertical in a girdle-like shape (Jacka and Maccagnan, 1984). In addition, diffusional creep and grain boundary sliding have been considered by some authors, offering the possibility of grain-size-sensitive deformation mechanisms (Goldsby and Kohlstedt, 1997, 2001; Cuffey and others, 2000; Faria and others, 2006). These impurity effects of the ice flow have been identified in deep ice cores like Dye 3 (Dahl-Jensen and Gundestrup, 1987; Shoji and Langway, 1987), GRIP (Miyamoto and others, 1999), EDC (Durand and others, 2009), WAIS (Fitzpatrick and others, 2014), EPICA-DML (Faria and others, 2006, 2009, 2010; Weikusat and others, 2017) or NEEM (Montagnat and others, 2014).

Ice microstructure in mountain glaciers

Microstructure analyses have been usually carried out in polar regions (Greenland and Antarctica ice sheets), whose thickness can surpass 4000 m, providing the opportunity to study the long-term evolution of deep ice layers under stable temperature and stress conditions and perform paleoenvironmental reconstructions up to 800 000 years (EPICA Community Members, 2004; Jouzel and others, 2007). In contrast, conducting the same type of microstructure studies on mountain glaciers is much less common, as it involves more technical difficulties due to their steeper topography and smaller volume, which imply shorter time series, a more heterogeneous deformation and a higher sensitivity to seasonal temperature variations and global warming. Strong temperature variations hinder microstructural studies because they can trigger thermodynamic processes that continuously modify the ice microstructure and fabric (e.g. dynamic recrystallization), especially in glaciers located in temperate regions. However, thanks to their sensitivity, mountain glaciers are excellent regional records of environmental variations of proxies like air temperature, precipitation, atmospheric chemistry, etc. (Dyurgerov and Meier, 2000; Grunewald and Scheithauer, 2010; Marshall, 2014). Furthermore, these glaciers are good indicators of the effects of past and current human activities, since they are usually close to densely inhabited regions (Zhang and others, 2015).

Regarding studies focused only on ice microstructure or fabric in mountain glaciers, one of the first works was by Perutz and Seligman (1939), which investigated the glacier structure and flow mechanisms of the Great Aletsch glacier. Twelve years later, Rigsby (1951) analysed the ice fabrics of an ice core extracted from Emmons Glacier (Washington, USA) and used the results some years later in a comparative study that included glaciers from different climatic contexts, such as the Malaspina Glacier (Alaska), Saskatchewan Glacier (Alberta, Canada), Moltke Glacier and the Nunatarssuaq and Tuto ice ramps near Thule (Greenland; Rigsby, 1960). A coetaneous study is the fabric analysis of Blue Glacier (Olympic National Park, Washington state; Kamb, 1959). In recent decades, we can highlight studies on the Tsanfleuron Glacier (Switzerland; Tison and others, 2000), Cole Gnifetti Glacier (Swiss-Italian Alps; Kerch, 2016), Storglaciären glacier (Sweden; Monz and others, 2021), Rhone Glacier (Swiss Alps; Hellmann and others, 2021), an ice apron in the Triangle du Tacul (Mont Blanc Massif; Guillet and others, 2021) and Jarvis Glacier (Alaska; Clavette, 2020). However, most works focus only on the fabrics, superficially describing other microstructural features like the shape, size and interactions between grains.

Our research group is part of a network whose aim is the study of the Monte Perdido Glacier. In this context, we are contributing by characterizing, for the first time, the microstructure of its ice, looking at the interaction between its elements (i.e. grain boundaries; GB, sub-grain boundaries; sGB, bubbles and impurities). For this we used high-quality photos and micrographs, cross-polarizers observations and transmitted light microscopy. In this study, we focus on a section of the central part of an ice core drilled in the lower accumulation zone of the glacier, characterized by its high impurity content.

Study area

Monte Perdido Glacier (42°40′50″N, 0°02′15″E), located in the Ordesa y Monte Perdido National Park (Central Spanish Pyrenees; Fig. 1a), is the third largest glacier in the Pyrenees (0.37 km^2 in 2016; Rico and others, 2017), although recent studies have reported a 12.9% area loss from 2011 to 2020 (Vidaller and others, 2021). The glacier lies on the northern slope of the Monte Perdido Massif, below its main summit (3355 m a.s.l.; Fig. 1b). The thickness varies from 30 to 50 m in the best-preserved areas of the glacier (López-Moreno and others, 2019). The Glacier's meltwater drains via the Cinca River, which flows through a longitudinal (E-W) basin called Tucarroya Cirque (5.8 km^2) that bonders the Tucaroya Ridge and Eastern Astazu Peak (3071 m a.s.l.) on the north, the Western Astazu Peak (3013 m a.s.l.) on the west and an immense cliff of 500–800 m (García-Ruiz and Martí-Bono, 2002), composed by the Monte Perdido Peak (3355 m a.s.l.), Cilindro Peak (3322 m a.s.l.) and the Marboré Peak (3247 m a.s.l.) on the south (Fig. 1b). Currently, the glacier is formed by two bodies: the upper one and the lower one, with average elevations of 3110 and 2885 m a.s.l., respectively (Julián and Chueca, 2007). The climatic context is high-mountain Atlantic-Mediterranean transition, with a mean annual temperature of 5°C (measured at Góriz station, 2250 m a.s.l., 2.7 km from the glacier, on the south face), and a mean summer temperature (June–September) measured at the foot of the glacier in the period 2014–2017 of ~7°C (López-Moreno and others, 2019). Assuming a temperature drop of 0.55–0.65°C every 100 m, the average annual elevation of the 0°C isotherm is at ~2945 m a.s.l., involving a small or even non-existent accumulation area during warm years (López-Moreno and others, 2019). Snowfall events can occur at any time of the year, but generally, the accumulation process takes place from November to May, and the melting extends from June to September (López-Moreno and others, 2016). Despite the elevation of the upper section, the low avalanche activity and the high slope of ~40° limit the snow accumulation (López-Moreno and others, 2019). Results of chronological analyses carried out by Moreno and others (2021) showed that the glacier's ice record covers the last 2000 years. The Little Ice Age (LIA) period, characterized by glacial advances, is not recorded in the Monte Perdido Glacier ice, since more than 600 years of accumulated ice have been lost due to the anthropogenic warming that followed the LIA.

Materials and methods

In the fall of 2017, three vertical ice cores were recovered from the glacier's lower section (Moreno and others, 2021 and Fig. 1b). The

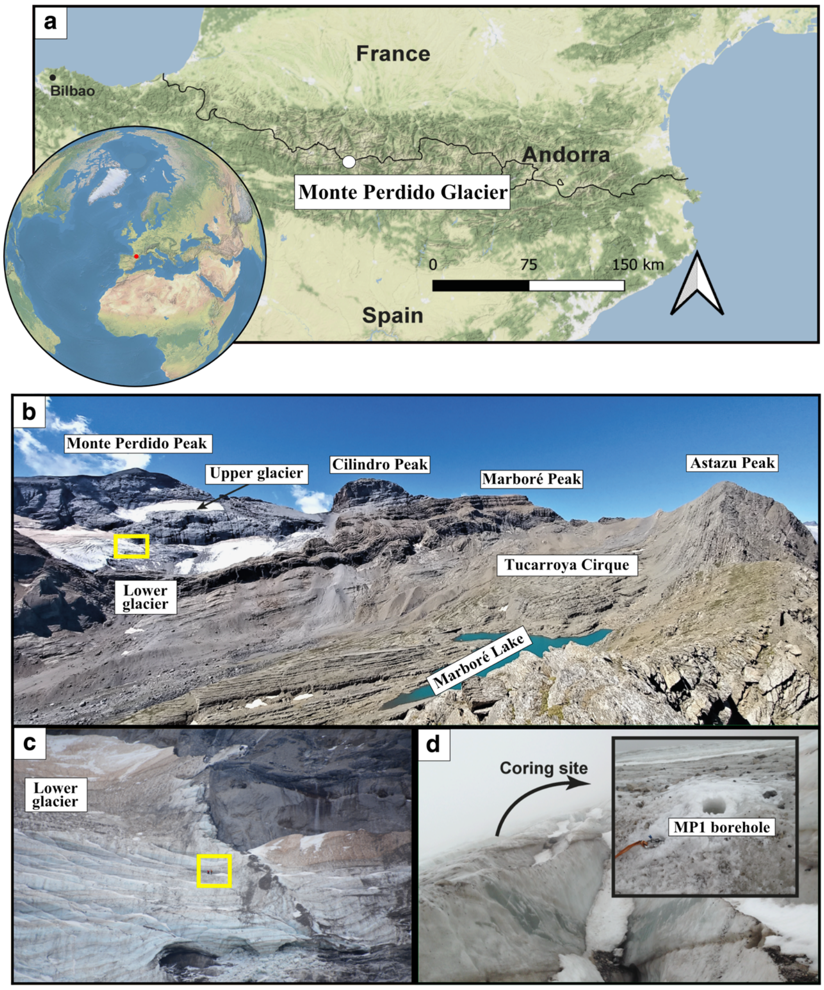

Figure 1. The red dot indicates the location of the Monte Perdido Glacier. (a) Geographical situation of Monte Perdido Glacier in the Pyrenees. (b) Main peaks in the Marboré Cirque. The yellow box indicates the MP1 ice core extraction site. (c) Zoom into the yellow box of Figure 1b. Brownish areas on the top-right and centre-left parts of the figure are the result of mineral dust deposition events. The rocky outcrop on the right is composed of Paleocene limestones. (d) Detail of the MP1 borehole after extraction.

microstructural analyses were carried out at the low-temperature laboratory *IzotzaLab*, located at the Basque Centre for Climate Change (BC3). The ice cores were stored in a chest freezer at −70°C to limit the microstructural changes triggered by the increases in temperature. During the analyses, the conditions at the laboratory were −25°C and 45% RH. One of the ice cores belongs to the end of the accumulation zone, very close to the equilibrium line (MP1; 42°40′47.7″N, 0°02′15.9″E; Fig. 1d), with a total depth of 410 cm and consisting of several segments (labelled downward from MP1–1 to MP1–11). The dominant structure throughout the MP1 core is that of bubbly ice, with some unclear vestiges of firn in certain layers. The target segment (MP1–6) was made of two sections (the upper one, S_1, and the lower one, S_2) with a total length of 22.6 and 8 cm in diameter, comprising a depth range between 251 and 273 cm within MP1 (Fig. 2a).

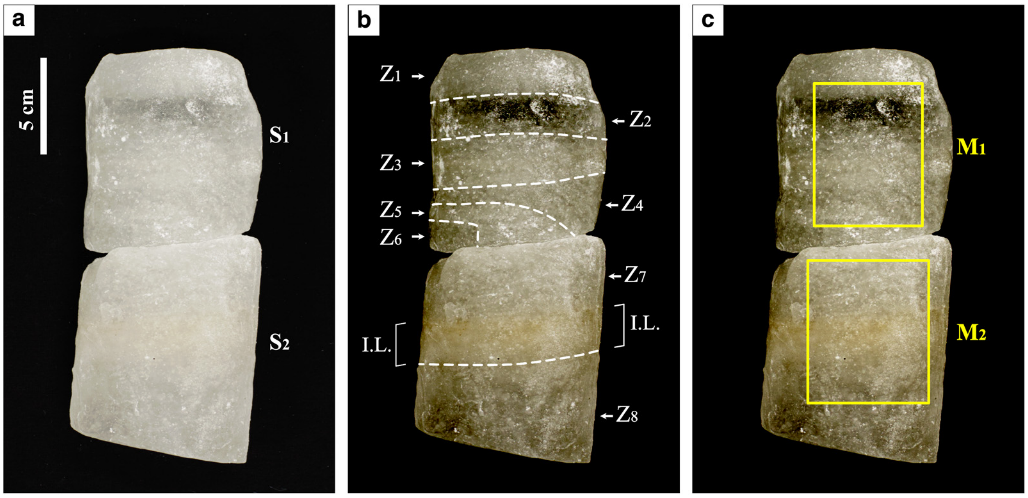

Figure 2. MP1–6 segment. (a) MP1–6 lower (S_1) and upper (S_2) sections. (b) Zones (Z) with different bubble number densities delimited by dashed lines. In the lower section, the impurity layer (I.L.) is visible. (c) Position of M_1 and M_2 samples.

https://doi.org/10.1017/aog.2023.66 Published online by Cambridge University Press

Visual stratigraphy

For describing ice features like bubble distribution, ice appearance, or layers with different colouration (e.g. cloudy bands), we photographed the ice core using a zenithally arranged digital camera, a black backdrop and scattered lateral illumination. The picture's output format was 'raw', allowing subsequent image processing. Due to the high light scattering produced by the air bubbles, it is hard to identify the ice core's internal features in the visual stratigraphy (Fig. 2a). To solve this problem and reveal the ice-core inner features, we adjusted the RGB channels simultaneously, decreasing the mid-tones brightness level and increasing the contrast with the Affinity Designer™ image software (Fig. 2b). Using a bandsaw (Metabo™ BAS 318), we prepared the samples for cross-polarized and microstructural observations, one from the central part of S_1 (M_1) and another from S_2 (M_2; Fig. 2c).

Observations between crossed polarizers

To determine the polycrystalline natural ice fabric, we can use an optical approach based on ice crystals' birefringence and extinction angle (Rigsby, 1951; Langway, 1958; Kamb, 1959). The birefringence colour of each grain depends on the *c*-axes orientation, allowing us to distinguish the grain's outlines. For this analysis, we fixed samples to the sample holder with water droplets (water acts as a 'natural glue' at −25°C) and used a microtome (Leitz™ 1400) to polish the upper surface to eliminate the irregularities produced by the band saw. Then, we turned around the sample and repeated the same process on the other surface, polishing it until a thickness between 100 and 400 µm was reached, to reveal most of the grains through crossed polarizers. For the observation, each sample was placed between two linear polarizing films, the lower one fixed and the upper one rotated until the polarization directions were 90° to each other (cross-polarization).

Optical microscopy

A microstructural analysis is necessary to understand the grain size evolution and its variations due to interactions with other elements such as sGB, bubbles or impurities. Employing a Leica™ DM6M microscope set inside the *IzotzaLab*, we scanned the microstructure through transmitted light along bands (2.3 mm × 80 mm) parallel to core axis. The preparation process is similar to that used for the polarization samples, but with a thicker final thickness of 0.5 cm. Before observations, the samples' polished surfaces were subjected to a sublimation process to reveal the microstructure. Sublimation is more intense in the areas where the GB, sGB or point defects intercept the surface, due to their higher free energy. Besides, sublimation eliminates the surface grooves caused by the microtome blades, allowing a clearer observation. The sGB boundaries have shallower, greyish sublimation grooves (Saylor and Rohrer, 1999), unlike GB with higher contrast and a dark grey or nearly black colour. The microstructural elements observable by this method are known as *surface elements*, and when we move the focus towards the sample inside, they become blurred. By contrast, the interior elements are located inside and are not sublimation products (e.g. slip bands, air bubbles or impurities; Kipfstuhl and others, 2006; Faria and others, 2018). The time and quality of sublimation depend on the laboratory environmental conditions (temperature, temperature gradient, humidity and air velocity just above the sample surface). To accelerate this thermodynamic process, the sample can be placed under a light bulb or a dry air stream. The microscopy method described above has been widely used in glaciology (e.g. Mullins, 1957; Nishida and Narita, 1996; Kipfstuhl and others, 2006). One characteristic of our samples is they have levels with high air bubble content. When we try to observe these samples with the transmitted light microscope, the bubbles appear as black regions, making it hard to distinguish the surface elements, even using a specialized software. Therefore, for better visualization of these elements, we had to resort to a hand-drawn outlining of the GB, sGB and bubbles (e.g., Figs 3–5).

Chemical analysis

To perform a preliminary chemical characterization of the crystalline species of the impurities inside S_2, we extracted a 3 cm^3 sample from the central part of M_2 and placed it inside a Petri dish.

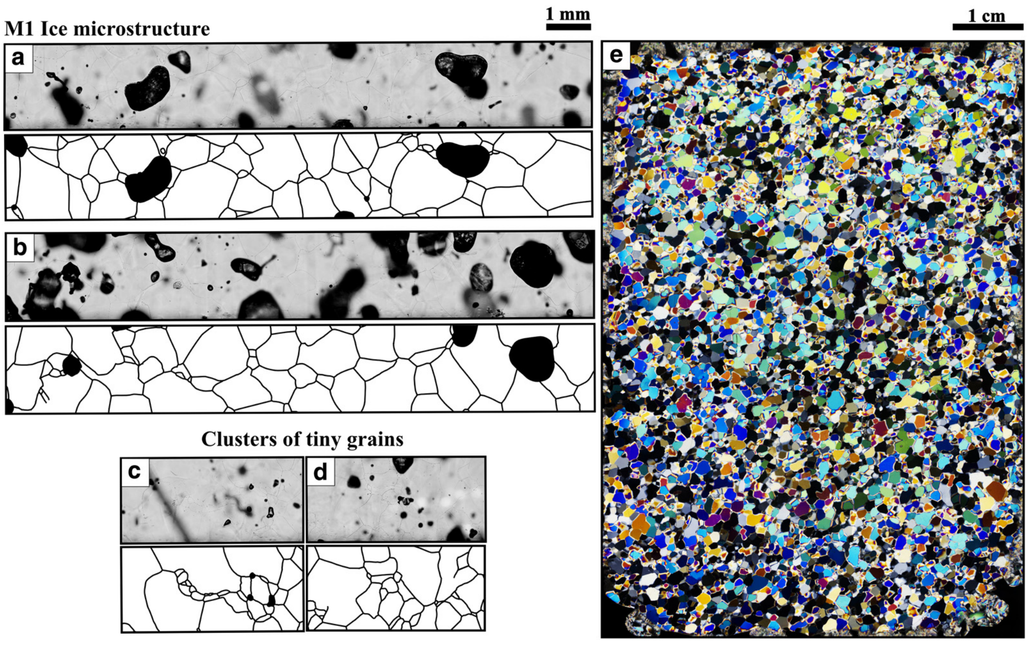

Figure 3. M_1 ice microstructure. To improve the visualization of grain size and shape, the grain boundary (GB) outline is depicted below each scanned band, including also the parts of bubbles exposed to the surface (in black). (a) and (b) Micrographs representing the sample's general appearance. (c) Nucleation of tiny grains along a GB. (d) Cluster of tiny grains, possibly an example of particle-stimulated nucleation (PSN) process. (e) Detail of M_1 under crossed polarizers.

https://doi.org/10.1017/aog.2023.66 Published online by Cambridge University Press

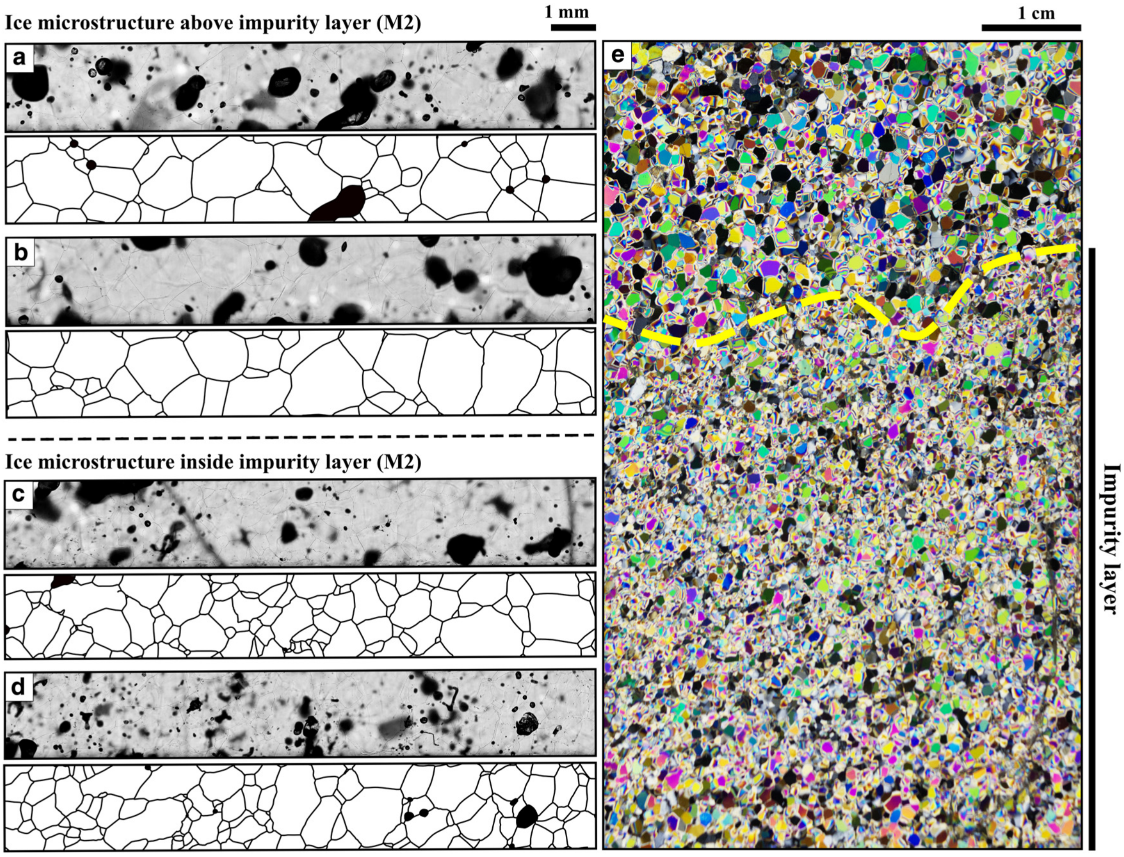

Figure 4. M_2 ice microstructure. The dashed black/yellow lines represent the upper limit of the impurity layer. (a) and (b) Microstructure of the upper part of the sample, where the impurity concentration is low. (c) and (d) Microstructure within the impurity layer. (e) Detail of M_2 under crossed polarizers.

Subsequently, the sample was melted and evaporated inside a stove at 30°C, partially covered with aluminium foil to avoid external contamination and to allow the water vapour to escape. The chemical analyses consisted of Raman spectroscopic characterization of the precipitated salts and the original impurities remained at the bottom of the Petri dish. The instrument used was the Renishaw inVia confocal micro-Raman spectrometer (Renishaw, UK), which is calibrated daily using a standard silicon slice. Although analyses were carried out with all lasers (785, 633 and 523 nm), the 532 nm diode laser (Renishaw UK RL532C50 with a nominal 300 mW output power) brought the best results. The Micro-Raman spectrometer is also equipped with a CCD detector cooled by the Peltier effect, with a LEICA DMLM microscope (Bradford, UK), which employs an XYZ Stage Control toolbar and a micro camera to explore the target particles. For visualization and focusing, we used the 5× N PLAN (0,12 NA) and 20× N PLAN EPI (0,40 NA) objectives.

Results

In MP1–6, variations in bubble number density (ρ_{bn}) and impurity content define the stratigraphy, but the stratigraphic boundaries defined by bubbles and impurities do not always coincide. The zones with high ρ_{bn} values can be identified by a whitish appearance, in contrast to the low-density zones, where the ice is more translucent and has a dark aspect due to the dark background. We could identify eight zones of high and low ρ_{bn} values, labelled from Z_1 to Z_8 (Fig. 2b). The zones Z_1, Z_3, Z_5 and Z_7 have higher value than Z_2, Z_4, Z_6 and Z_8, being Z_2 the zone with the lowest density. The impurities only define a single reddish-brown layer located in the middle part of S_2, with a thickness of ~3 cm and a tilt of ~10°. Its limits are not well-defined, and the lower limit coincides with the transition between Z_7 and Z_8. It is noteworthy to mention that we are reporting 2D descriptions of structural characteristics with volumetric (3D) variations, so this is only an approximate view. The distribution of bubbles and impurities will vary depending on the observed section.

To analyse the morphological characteristics of the bubbles, we photographed two samples previously prepared for the microscopic observation, named M_1 (extracted from S_1) and M_2 (from S_2), as indicated in Figure 2c. Both samples belong to the central part of each section and are parallel to the ice core axis. Generally, M_1 has bubbles in greater number and size than M_2. We could identify eight domains of different bubble morphological characteristics in both samples, labelled from D_1 to D_8, each one characterized by differences in bubble shape, size and ρ_{bn} values (Fig. 6; Table 1). Domains 2 (D_2) and 8 (D_8) had the smallest and most rounded bubbles, coinciding with the fact that they are areas with the lowest ρ_{bn} values. The pattern of bubbly size and shape observed in D_2 spreads homogeneously across M_1 and M_2. A remarkable feature of D_8 is its morphology because it forms an indentation (notch shape) towards the interior of D_7, with a higher bubble number density. Over the upper limit of D_8, there are clusters with high ρ_{bn} values (Fig. 6b). In the rest of the domains, bubbles with irregular morphologies prevail, and from D_4 to D_7, it seems like bubbles have coalesced, generating larger compound bubbles. There are some correspondences with the visual stratigraphy: D_2 correlates directly with Z_2, while Z_4 can be related to D_5. In the other zones, there is no apparent correlation with domains.

Observations through crossed polarizers revealed the grains that make up both samples, allowing the analysis of their morphology and size. The sample thickness determines the dominant birefringence hue, and the colouration of each grain reveals

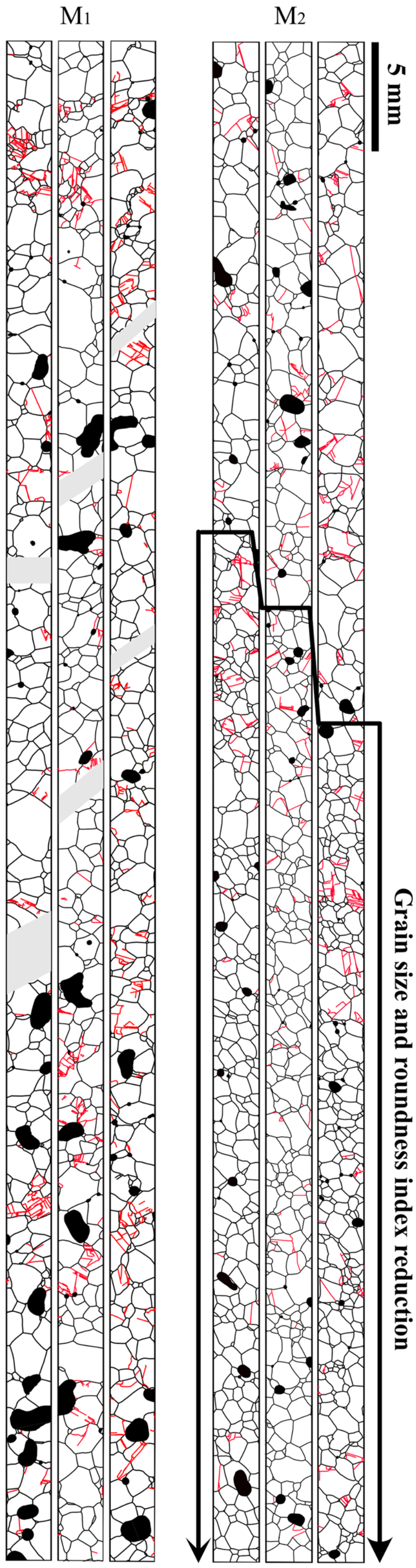

Figure 5. Microstructure outlines of the M_1 (Right) and M_2 (left) micrographs. Grain boundaries (GB, black lines), sub-grain boundaries (sGB, red lines) and bubbles (black areas). Grey rectangles represent regions where the sample microstructure is damaged by fractures. The stepped black line represents the upper limit of the impurity layer in M_2. Below it, there is a decrease in grain size and roundness index.

variations in the directions of the *c*-axes. Although birefringence hues in M_1 and M_2 are different (Figs 3e, 4e), the colour distributions of the grains in both samples suggest a nearly isotropic ice fabric. Concerning grain size, we identified two main grain groups:

- ***Group 1 (G_1)*** encompasses big grains, whose boundaries and birefringence colours are well-defined (Fig. 3e).
- ***Group 2 (G_2)*** includes smaller grains without well-defined boundaries or birefringence colours due to grain edge interference, presenting an iridescent appearance (central and lower part of Fig. 4e)

Aspect differences between these two groups are directly related to grain size and samples' thicknesses. In G_1, the grains are larger than the sample thickness, so we observed a section of almost every single grain. In G_2, the grain size is smaller, so there is more than one grain within the total sample thickness. Owing to these dissimilarities, we used cross-polarization photographs for G_1 and microscopy photographs for G_2. On the one hand, G_1 grains are dominant in M_1, although the distribution of both groups is homogeneous throughout the sample. On the other hand, G_1 only prevails in the upper third of M_2 because G_2 is dominant in the central and lower part of the sample. The average grain size of G_1 is similar in both samples (0.104 mm^2 in M_1 and 0.138 mm^2 in M_2), while the shape is roughly polygonal with a roundness index (inverse of the aspect ratio) of 0.79 in M_1 and 0.87 in M_2. Group 2 (G_2) has an average size of 0.006 mm^2 (two orders of magnitude smaller than G_1) and a roundness index of 0.67, the smallest value of the entire sample set. Grains belonging to G_1 inside the zone of the predominance of G_2 have similar size compared to the rest of the sample (0.132 mm^2), but the roundness is smaller, with a value of (0.75; Table 2).

Regarding chemical analyses (Fig. 7), the first crystalline compound identified in the M_2 micro-Raman analysis was Quartz [SiO_2] due to its characteristic bands using different laser intensities: very weak (295 cm^{-1}), weak (262 and 396 cm^{-1}), medium (131, 209 and 358 cm^{-1}) and very strong (467 cm^{-1}; Huidobro and others, 2021). Anatase [TiO_2] was also occasionally detected thanks to its most characteristic Raman band at 144 (vs) cm^{-1} (Huidobro and others, 2021). Finally, atacamite [$Cu_2Cl\ (OH)_3$] was also recognized several times. Although this mineral has several Raman patterns, the principal Raman bands always appear at the same positions: 155 (vs), 266 (m), 289 (strong, s), 335 (w), 374 (w), 455 (m), 477 (m), 513 (s) and 808 (vw) cm^{-1} (Marcaida and others, 2019; Li and others, 2020).

Discussion

The origin of ice layering

Variations in grain size and shape, bubble number density (ρ_{bn}) and impurity concentration may define an ice stratification (Allen and others, 1960; Hambrey, 1975, 1977; Hambrey and Milnes, 1977; Hudleston, 1977). The stratification defined by ρ_{bn} can be *primary* (i.e. *sedimentary*) or *secondary* (also called *foliation*). The origin of primary stratification lies in the snow accumulation parallel to the glacier surface and its subsequent transformation into firn and ice (Lewis, 1960; Hambrey, 1976, 1994; Hambrey and Lawson, 2000). In general, this stratification generates isochronous layers and it is common in glacier accumulation zones, meaning above glaciers' equilibrium-line altitude (ELA). The different characteristics of the layers can reflect the environmental (atmospheric) conditions that prevailed at the time of the snow deposition (e.g. seasonal variations), as well as the post-depositional processes that could have affected the snowpack or glacier ice (e.g. Schytt, 1955; Shumskii, 1964; Wadham and Nuttall, 2002). In this vein, in glaciers that used

https://doi.org/10.1017/aog.2023.66 Published online by Cambridge University Press

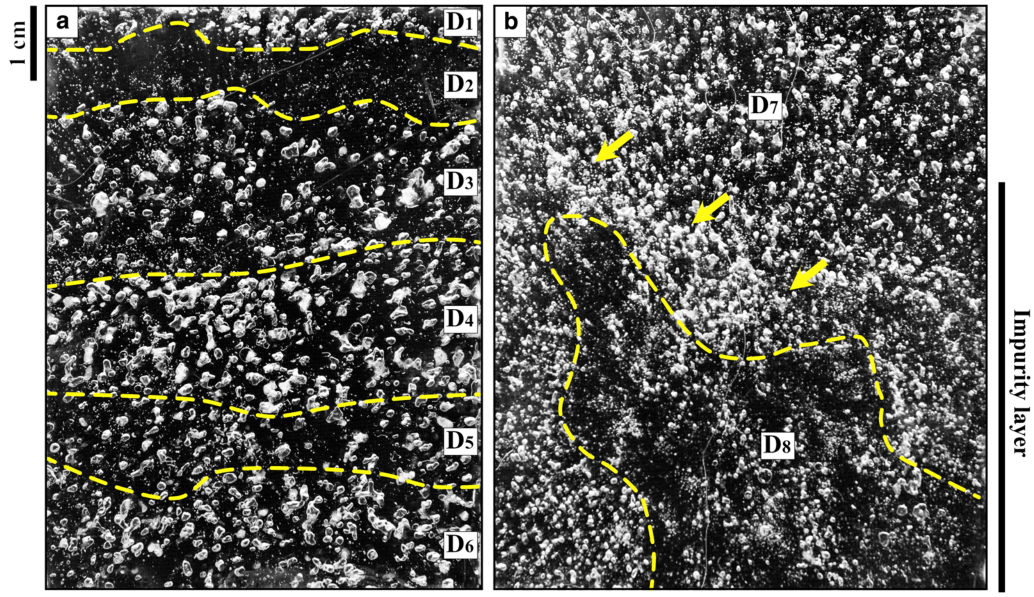

Figure 6. Domains (D) with different values of bubble number density (ρ_{bn}), sizes and shape, delimited by the yellow dashed lines. (a) M_1 sample. (b) M_2 sample. Arrows indicate zones with high ρ_{bn} values.

Table 1. Air bubble morphological characteristics in the ice samples M_1 and M_2

Sample	Domain	Average bubble size (mm^2)	Morphology	Bubble counting
M_1	D_1	0.9	Irregular	35
	D_2	0.045	Round	200
	D_3	1.6	Irregular	80
	D_4	2.3	Interconnected	200
	D_5	2.3	Interconnected	200
	D_6	2.3	Interconnected	200
M_2	D_7	0.8	Interconnected	200
	D_8	0.4	Round	200

Table 2. Grain size and roundness in the ice samples M_1 and M_2

Sample	Group	Average grain size (mm^2)	Roundness	Grain counting
M_1	G_1	0.104	0.79	1,532
M_2	G_1	0.138	0.87	838
	G_1 inside the impurity layer	0.132	0.75	284
	G_2	0.006	0.67	608

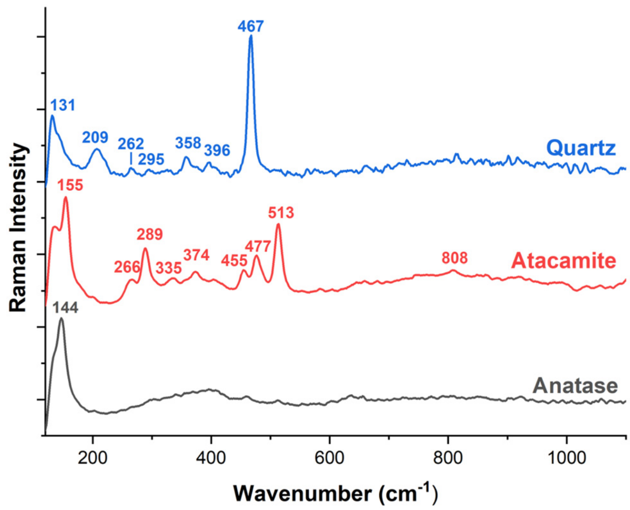

Figure 7. Micro-Raman analyses of the M_2 impurity layer. Quartz (SiO_2 polymorph; blue line), atacamite ([Cu2Cl (OH)$_3$]; red line) and anatase (TiO_2; grey line).

to suffer partial melting and refreezing (e.g. temperate glaciers like Monte Perdido Glacier), layers with high ρ_{bn} values may represent the winter season. Conversely, layers with a transparent appearance (low ρ_{bn} values) could indicate of the summer season, and are usually located at the base of the snowpack or at different firn depths, where they acquire a lenticular morphology (Hambrey, 1994; Hambrey and Lawson, 2000). Besides, porosity and other void-space characteristics may be useful indicators of the transition zone between firn and bubbly ice. The transition of this depth differs between temperate glaciers, where there is a significant influence of melting and refreezing processes creating a complex stratigraphy (Kawashima and Yamada, 1997), and glaciers in polar areas, where the transition occurs in a more ordered and gradual fashion, mostly in a dry state (Alley and others, 1982).

Secondary stratification is directly related to the ductile deformation of ice and is responsible for variations in the distributions of size, shape and position of grains and bubbles. The higher the deformation, the more intense and marked the foliation (Barnes and Tabor, 1966; Hambrey and Milnes, 1977; Hooke and Hudleston, 1978; Brepson, 1979; Hambrey and others, 1980). Foliation forms perpendicular to the maximum compressive stress (Glen, 1956; Meier, 1960; Hooke and Hudleston, 1978; Pfeffer, 1992), which in case of well-developed simple shear leads to foliation arranged parallel to the shear plane (Chamberlin and Salisbury, 1909; Perutz and Seligman, 1939; Ragan, 1969). Thus, this particular type of air-bubble layering may reflect decadal-scale deformation processes in temperate glaciers or even millennial-scale in polar ice sheets (e.g. Paterson, 1994).

Based on this information and the results of our analyses, in the following sections, we will try to find out the possible origin of the layering that characterizes the MP1–6 section, defined by ρ_{bn} and impurities.

https://doi.org/10.1017/aog.2023.66 Published online by Cambridge University Press

Primary origin

For the first argument, it is necessary to consider the annual mean altitude of the 0°C isotherm (2945 m a.s.l.; López-Moreno and others, 2019) and the glacier's ELA (3050 m a.s.l.; López-Moreno and others, 2016). The MP1 ice core was extracted at ~2900 m a.s.l., meaning in the upper limit of the ablation zone (Figs 1b, c). However, it is not a well-defined boundary and exhibits natural spatial variability. Therefore, the characteristic processes of the accumulation zone may influence the drilling site. If we consider this possibility valid, the levels with lower and higher ρ_{nb} values likely represent the summer and winter seasons, respectively.

Second, in our samples, there is no preferential elongation of the crystals (Figs 3, 4) nor the bubbles (Fig. 6), which could exclude the presence of deformation processes. Instead, the samples show ice crystals with a predominantly polygonal shape, while the bubbles display circular or irregular morphologies. For example, researchers observed crystal elongations in glaciers like Storglaciären (Sweden; Hudleston, 2015), and in the case of air bubbles, samples of glaciers located in cold regions exhibit typical deformation morphologies (Gow, 1968; Hudleston, 1977; Alley and Fitzpatrick, 1999).

The third piece of evidence derives from the micro-Raman results (Fig. 7). The chemical composition of the three main minerals (i.e. atacamite, anatase and quartz) is consistent with previous chemical studies. Moreno and others (2021) reported that the Al-normalized enrichment factors of Ti, Mn, Cr, Co, Ni, Cu and Pb are higher compared to the concentrations measured at the Ordesa monitoring station (8 km from the glacier and 1190 m a.s.l.), with Cu and Pb presenting a higher enrichment factor (>6). Moreover, the characteristically high values of Cu/Mn, As/Se and Pb/Zn ratios indicate a significant impact of Cu mining and smelting activities (Corella and others, 2018). In Bielsa Valley, these activities were active during pre-industrial periods (Callén, 1996), like the former Parzán mines, one of the main lead and silver deposits of the Central Pyrenees, located 7 km westward from the glacier. However, as this is a preliminary study, more robust analysis and results are needed to clarify questions such as the origin of the atacamite, i.e. it can be primary or a product of oxidation processes of other copper minerals.

Moreno and others (2021) found that detrital-rich laterally extended layers define a primary stratigraphy, identifiable in some areas of the glacier's lower section surface. The particle size ranges from silt (0.002–0.05 mm) to sand (0.05–2 mm), and these particles may have been transported to the glacier surface by wind (e.g. black carbon or dust) or are the result of erosion processes of local outcrops (e.g. frost weathering). Levels with high impurity concentration can reveal episodes of reduced ice accumulation or periods dominated by ablation, as the particles concentrate in specific layers due to the ice melt, promoting the formation of darker-coloured layers.

The most detected mineral in the analyses was quartz (a SiO_2 polymorph). Its origin may be weathering processes over local lithologies like the sandstones of the Marboré formation (Robador and others, 2020) or the deposition of mineral dust on the glacier surface. However, there are no sandstone outcrops nearby, increasing the likelihood of mineral dust. Dust particles are usually below tens of micrometres and incorporated into the atmosphere as an aerosol from arid or semi-arid regions, travelling long distances until deposited back to the surface. The composition consists mainly of a mixture of quartz, carbonates, iron oxides, clay minerals, sulphates and feldspars (Engelbrecht and others, 2016), whose relative abundances vary depending on the source area (Caquineau and others, 2002; Scheuvens and others, 2013; Formenti and others, 2014), accounting for 40% of annual aerosol emissions (IPCC, 2013). The North African region (Sahara and Sahel) is the main dust contributor worldwide (Prospero and others, 2002). Pyrenees act as a natural barrier for air masses coming from North Africa, making dust deposition higher in this region than in areas located hundreds of kilometres south (Pey and others, 2020). African dust-loaded air masses reach this mountain range 10% of the annual days (Pey and others, 2013), and the aerosol deposition is greater in cold seasons (from November to April), periods in which there is a predominance of extreme dust events coming from the north African desert (Fig. 1c). Pey and others (2020) estimated that concentrations of mineral dust in the Pyrenees vary between 4.5 and 10.6 g m^{-2}. On the one hand, during these events, particle composition has a mineral signature characterized by clay minerals and quartz, followed by feldspars, carbonates and hematite. On the other hand, in the absence of this phenomenon, the particles have a marked organic nature (Pey and others, 2020).

Considering the need for more chemical analyses, the impurities' horizontal arrangement in a layer-like disposition, the reddish colouration (possibly due to the presence of clay minerals) and the high quartz content, we could hypothesize that this layer is made up of mineral dust particles. Besides, if we combine the fact that mineral dust deposition events are more common in winter and that this impurity layer in S_2 is inside a zone with high ρ_{bn} values (indicative of winter, if we consider a primary origin), we could say (with caution) that this layer is indicative of a winter season with a high frequency of mineral dust deposition events (Fig. 2b). Additionally, we cannot exclude the possibility that this layer resulted from a succession of particle reconcentration events during a period characterized by high ablation rates or low snow accumulation.

Finally, cross-polarizer photographs support the last argument for the primary origin. At this point, it is important to emphasize that these interpretations are based on the assumption that variations in the birefringence colours are qualitative approximations of changes in the crystallographic *c*-axes arrangement. Both samples have an average thickness between 200 and 400 µm, and their birefringence hues are different and homogeneously distributed along each sample, without clusters of any particular colour, hinting that there are no significant changes in the fabrics related to the layering defined by the bubbles or by the impurities (Figs 3e, 4e). If we were dealing with a secondary origin, we would expect changes in the *c*-axis arrangement in regions where, as a result of shear stresses, basal slip planes tend to be parallel to the shear plane. Moreover, it has been often observed that inside impurity layers, there is a greater tendency for *c*-axes to approach a single maximum (Paterson, 1991), creating more favourable conditions for ice deformation and flow.

Bearing in mind these facts, we may be facing two possible scenarios: first, nowadays, there are no active deformation processes in the Monte Perdido Glacier, although such processes could have been active in the past. Second, deformation processes could be currently active, but are not strong enough to produce significant changes in the ice fabrics, at least on the level of the qualitative analysis we are working with. In both cases, since it is a temperate glacier, it is exposed to relatively high temperatures that cause recrystallization processes that may obliterate the original fabric deformation signs. For example, recrystallization can entail changes from a single maximum parallel to the foliation plane pole to an arrangement of three or four maxima, with none of them parallel to the foliation plane normal (Rigsby, 1960). Bader (1951) and Rigsby (1951) established the existence of these peculiar fabrics, and subsequent work by Schwarzacher and Untersteiner (1953), Rigsby (1953) and Meier and others (1954) provided new data supporting this investigation, as well as more uncertainty levels.

https://doi.org/10.1017/aog.2023.66 Published online by Cambridge University Press

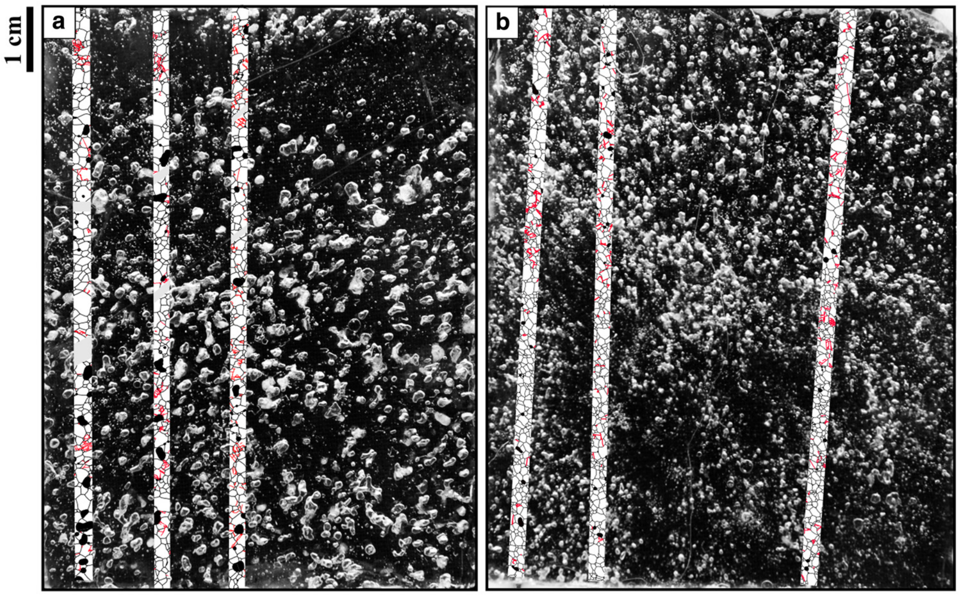

Figure 8. Detailed positions of the microstructure outlines in M_1 (a) and M_2 (b) depicted in Figure 5.

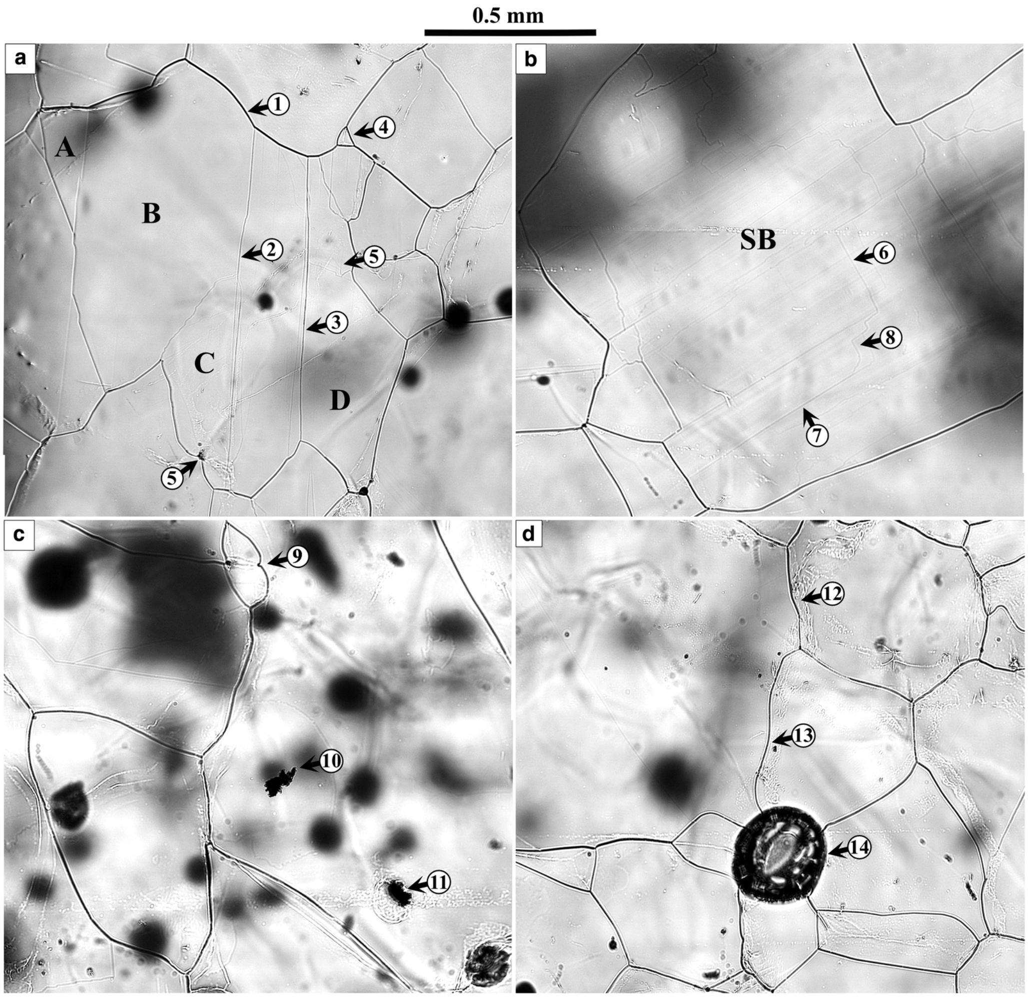

Figure 9. Micrographs of M_1 and M_2. (a) The image shows an ice grain delimited by its boundaries (GB; 1), which appear as black or dark grey lines. Inside, several sub-grain boundaries (sGB; e.g. 2 and 3) with a lighter appearance, reveal heterogeneous stresses within the grain. With time, sGB will evolve into GB, therefore multiple grains (A, B, C, D) will differentiate from the original grain (rotation recrystallization; RXX). Additionally, nucleation of a small grain at a GB triple junction (SIBM-N; 4) and dislocation walls (5) which will eventually merge and form an sGB, can be observed. (b) Throughout the grain surface, encompassing most of the micrograph, slip bands (SB; faint and parallel lines) also indicate shear stresses acting on the grain. Besides, examples of different types of sGB: *n* (6), *p* (7) and *z* (8) can be identified. (c) Points 9 and 5, the latter from Figure 9a, exemplify the pinning effect of micro-bubbles (9) or particles (5). Two irregular and opaque particles composing the impurity layer (10 and 11) are also visible. (d) Grain boundaries with sinusoidal shape (12 and 13) and bubbles (14) at the M_2 impurity level.

https://doi.org/10.1017/aog.2023.66 Published online by Cambridge University Press

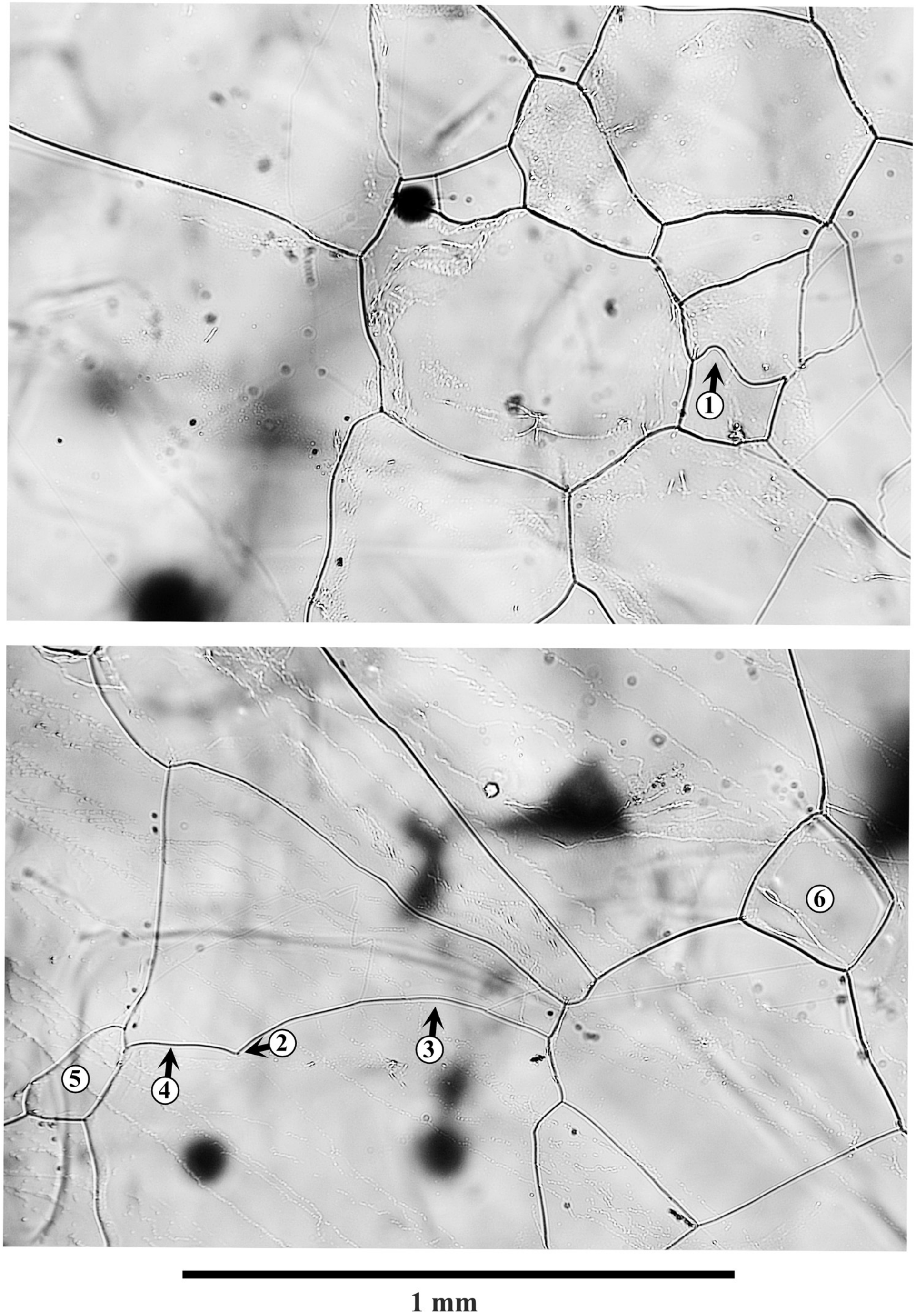

Figure 10. Regions where dynamic recrystallization dominates. Evidence of this process is the bulged grain boundaries, indicating the presence of SIBM-O (1, 3 and 4) or the nucleation of new grains SIBM-N (5 and 6). Additionally, point 2 is a clear example of the pinning process, in this case, caused by a micro-bubble.

Secondary origin

Combining the microscopy results, together with the high-resolution photos of the samples, we can observe how in M_1 the domains with low values of ρ_{bn} as D_2, or to a lesser extent D_5, there is a remarkable concentration of sGB (Figs 5, 8a), which could be indicative of heterogeneous deformation (thus, internal stress concentrations) at the microscopic scale (Weertman and Weertman, 1992; Figs 9a, b). Recent findings have quantified the ice velocity, concluding that the glacier has an average surface velocity of ~10 m a^{-1} (López-Moreno and others, 2019). Therefore, the sGB could indicate the stress and deformation produced by the ice flow. However, other parts with a low ρ_{bn} values, such as D_3 or D_8, do not present a preferential sGB concentration. There is even an opposite correspondence in the clusters with high ρ_{bn} identified between D_7 and D_8, where the sGB concentration is high (Figs 5, 8b). In the remaining zones, sGB are homogeneously distributed regardless of the number of air bubbles. Besides, there is a lack of direct correspondence between grain size and sGB, since the latter are present in both small grains of G_2 and larger grains of G_1.

The second argument relates the effects of the identified flow in the glacier and the occurrence of particles in the ice. When intense stresses act upon an ice grain, the strain energy tends to accumulate along the grain boundaries (GB), stimulating the formation of new grains along those regions (Humphreys and Hatherly, 2004). Additionally, this strain energy can concentrate around particles in the ice matrix, as they can hinder GB sliding, enhancing dynamic recrystallization and, ultimately, the

https://doi.org/10.1017/aog.2023.66 Published online by Cambridge University Press

nucleation of new grains (Song and others, 2005). This last mechanism is known as particle-stimulated nucleation (PSN), sooner identified in studies conducted on metals and alloys (Habiby and Humphreys, 1994; Huang and Humphreys, 2000; Somerday and Humphreys, 2003).

In our samples, we can find examples that illustrate both situations. On the one hand, we could identify small grains arranged along GB (Fig. 3c) in certain areas. On the other hand, in addition to the well-defined impurity layer in M_2, there are other regions throughout both samples where particles are present but at low concentrations, rendering them invisible to the naked eye and only detectable under the microscope. The zones where these particles form clusters correspond to round-like accumulations of tiny grains, whose occurrence could be a consequence of the PSN process (Fig. 3d). Both observations support the assumption that GMP ice may be subjected to sufficiently high stresses to trigger such deformation-induced phenomena.

By considering only the evidence that supports a secondary origin of stratification, implying the presence of glacier flow and combining it with the effects of impurities on this process, we encounter a scenario that facilitates an increase in ice-flow rates and deformation. If further comprehensive studies confirm the lateral extension of impurity layers along the glacier (i.e. affecting significant portions of the glacier), it could lead to a higher mass transfer rate from the upper regions of the glacier to the lower ones, specifically from accumulation zones to ablation zone. The visible and laterally extended impurity layers on the glacier's surface, reported by Moreno and others (2021), provide us with a clue about what we may discover at greater depths through the study of more ice cores.

Grain growth impurities interplay

In M_1, the particle concentration is low, and they are only perceptible under the microscope, unlike M_2, which has a noticeable level of impurities both in visual stratigraphy (Fig. 2b) and microscopy (Fig. 9c). In visual stratigraphy, this level has a characteristic brownish-red colour, while under the microscope, impurities appear as small opaque particles with irregular shapes and an average size of ≤0.05 mm. In addition to the impact these particles have on grain formation (previous section) they can interact with GB during migration (Beck and Sperry, 1950). The interaction mechanisms that can slowdown or even stop GB migration are known as *dragging* and *pinning*, respectively. In the lower section sample (M_2), we can observe what might be examples of these two mechanisms. In the middle and lower thirds of M_2, corresponding to the impurity layer, there is a drastic reduction in grain size and roundness index. Grain size decreases by two orders of magnitude, from average values of 0.12 mm^2 in M_1 and in the impurity-free zone of M_2, to 0.006 mm^2 within the impurity layer. The roundness index also experiences a decrease, from 0.83 outside the impurity layer to 0.67 within the layer (Figs 4c, d and 5).

In the M_2 impurity layer, there was no preferential concentration of particles along GB. Consequently, we did not observe any pinning effect. However, some GB show pinning processes produced by micro-bubbles (Figs 9c, 10). Despite the absence of particle-induced pinning, the correspondence between the impurity layer and grain size and roundness reduction is clear. Soluble impurities, which could affect GB motion through the drag effect, could explain this correspondence. Likely, evidence of this process is that even in the absence of particles (non-soluble impurities) at GB, a considerable portion exhibits a sinusoidal shape (Fig. 9d), indicating a potential reduction in migration velocity in some points.

At this point, it is essential to consider the resolution of the microstructural study, as we are only analysing three bands to observe the overall evolution of grain characteristics. To corroborate our observations and gain a better insight into the contribution of dragging and pinning effects, a more comprehensive analysis expanding the coverage (area) of microscopy would be necessary. This circumstance is similar in the upper 2300 m of EDML deep ice core (Antarctica), where it was also challenging to find a clear interaction between microstructure and particles (Faria and others, 2010).

Conclusions

This study is the first attempt to characterize the microstructure of the ice from the Monte Perdido Glacier, located in the Central Pyrenees, one of the southernmost glaciers in Europe. Analysing a specific segment (MP1–6), we studied the interactions between impurities and microstructure. One of the most noteworthy features of this segment is the stratification, defined by air bubbles and particles (non-soluble impurities). According to our results, this bubble-defined stratification presents evidence of both a primary (sedimentary) and a secondary origin (deformation-induced). Several factors support the primary origin: MP1 ice core belongs to the lower limit of the accumulation zone, there is no preferential elongation of bubbles or ice grains, the non-variation of birefringence colours along the samples indicates that there is no action of shear stresses, and finally, there is a correspondence between the layer with the maximum concentration of impurities (possibly resulting from Saharan dust deposition, more frequent in winter) and a zone with a high concentration of air bubbles (likely representative of the winter season). On the other hand, proofs supporting a secondary origin derived from some layers show a preferential concentration of sGB (microstructural elements indicative of heterogeneous deformation). Besides, the presence of clusters of tiny grains could be the consequence of the combination of deformation processes and the presence of particles. Both pieces of evidence indicate that the glacier ice is (or has been subjected) to higher stresses, possibly related to glacier flow. If we focus on the evidence supporting a secondary origin (linked to glacier flow processes) and combining it with the effects of the impurities on the natural ice mechanics (increase in flow/deformation), Monte Perdido Glacier could face a scenario of enhanced mass transfer from the accumulation zone to the ablation zone in the long term. This process would involve accelerated mass loss, particularly if the impurity layers extend horizontally.

Regarding the effect of impurities on microstructure, a clear inverse relationship is observed between their concentration and grain size/roundness. The combination of drag and pinning mechanisms, generated by the interaction between insoluble impurities (particles), soluble impurities and micro-bubbles with the GB migration process, could explain this correspondence. The dragging seems to be the prevailing process (as observed in the microscopy bands), whereas only a few GB exhibit pinning by micro-bubbles.

For a preliminary characterization of the particles, we employed a micro-Raman spectrometer. Using this technique, we identified atacamite and anatase, whose presence is consistent with past mining activities in the vicinity and previous chemical studies on the Monte Perdido Glacier. However, quartz was the predominant mineral, and its presence could be related to the arrival of dust-laden air masses from North Africa. If further analysis confirms with greater certainty that this impurity layer is made of mineral dust, it is essential to be aware that since the second half of the 20th century, there has been an increase in Saharan dust transport to Western Europe (Sousa and others,

https://doi.org/10.1017/aog.2023.66 Published online by Cambridge University Press

2019; Cruz and others, 2021), as a consequence of an average 10% increase in the extension of this desert between 1920 and 2013 (Thomas and Nigam, 2018). A greater input of mineral dust into the Pyrenees cryosphere would imply an increased likelihood of preserving some of these particles in the accumulation areas through their incorporation into the glacier ice structure (as likely happened in our study), increasing their influence on ice mechanics. Besides, mineral dust in the Pyrenees cryosphere reduces the albedo of the seasonal snow cover, accelerating its melting. Recent findings have shown that the albedo decreases during years with deposition events, ranging from 0.4 to 0.6 (e.g. 2016–2017), whereas in years without events, the albedo ranges from 0.7 to 0.9 (e.g. 2018–2019; Pey and others, 2020).

In addition to the role of impurities, other factors are reinforcing glacier degradation, such as the annual increase in regional temperatures (e.g. López Moreno and others, 2010; El Kenawy and others, 2012; Pérez-Zanón and others, 2017), the widespread predominance of ablation processes over accumulation events (López Moreno and others, 2019), and the decrease in thickness and surface area of the seasonal snow cover during the second half of the 20th century, especially at lower elevations (López-Moreno and others, 2005, 2009).

Acknowledgements. This research was supported by the Spanish Government through the María de Maeztu excellence accreditation 2018–2022 (MDM-2017-0714) and by the Spanish Agencia Estatal de Investigación (AEI Spain) through the projects PaleoICE EXPLORA (CGL2015-72167-EXP) and iMechPro (RTI2018-100696-B-I00). NGS acknowledges a PhD grant from the Basque Government (PRE-2018-1-0116). We thank the directorate of the Parque Nacional de Ordesa y Monte Perdido (Spain) for permission to investigate the Monte Perdido glacier. We also thank Ibai Rico (https://basquemountainguides.com/, UPV/EHU), Maria Leunda (UPV/EHU), and Juan Ignacio López-Moreno (IPE-CSIC) for their help during the sampling of the MP1 ice core, and Pedro Sanchez Navarrete (IPE-CSIC) for transporting the ice samples. Finally, we would like to extend our appreciation to the anonymous reviewers, the Scientific Editor, Christine Hvidberg, and the Chief Editor, Hester Jiskoot, for their valuable comments on this manuscript.

References

Allen CR, Kamb WB, Meier MF and Sharp RP (1960) Structure of the lower Blue Glacier, Washington. *The Journal of Geology* **68**(6), 601–625. doi: 10.1086/626700

Alley RB, Bolzan JF and Whillans IM (1982) Polar firn densification and grain growth. *Annals of Glaciology* **3**, 7–11. doi: 10.3189/S0260305500002433

Alley RB and Fitzpatrick JJ (1999) Conditions for bubble elongation in cold ice-sheet ice. *Journal of Glaciology* **45**(149), 147–153. doi: 10.3189/S0022143000003129

Bader H (1951) Introduction to ice petrofabrics. *The Journal of Geology* **59**(6), 519–536. doi: 10.1086/625909

Barnes P and Tabor D (1966) Plastic flow and pressure melting in the deformation of ice I. *Nature* **210**(5039), 878–882. doi: 10.1038/210878a0

Beck PA and Sperry PR (1950) Strain induced grain boundary migration in high purity aluminum. *Journal of Applied Physics* **21**(2), 150–152. doi: 10.1063/1.1699614

Brepson R (1979) Simulated glacier sliding over an obstacle. *Journal of Glaciology* **23**(89), 143–156. doi: 10.3189/S0022143000029798

Budd WF and Jacka TH (1989) A review of ice rheology for ice sheet modelling. *Cold Regions Science and Technology* **16**(2), 107–144. doi: 10.1016/0165-232X(89)90014-1

Callén JJN (1996) El proceso sidero-metarlúrgico altoaragonés: los valles de Bielsa y Gistain en la Edad Moderna (1565–1800), Llull. *Revista de la Sociedad Española de Historia de las Ciencias y de las Técnicas* **19**, 471–508.

Caquineau S (2002) Mineralogy of Saharan dust transported over northwestern tropical Atlantic Ocean in relation to source regions. *Journal of Geophysical Research* **107**(D15), 4251. doi: 10.1029/2000JD000247

Chamberlin TC and Salisbury RD (1909) *Geology: Geologic Processes and Their Results*. New York: H. Holt. Available at https://books.google.es/books?id=0fghAQAAMAAJ

Clavette R (2020) The microstructural heterogeneity of ice in Jarvis Glacier, Alaska. Honors College, University of Maine, 589. Available at https://digitalcommons.library.umaine.edu/honors/589

Corella JP and 8 others (2018) Trace metal enrichment during the Industrial Period recorded across an altitudinal transect in the Southern Central Pyrenees. *Science of the Total Environment* **645**, 761–772. doi: 10.1016/j.scitotenv.2018.07.160

Cruz JA, McDermott F, Turrero MJ, Edwards RL and Martín-Chivelet J (2021) Strong links between Saharan dust fluxes, monsoon strength, and North Atlantic climate during the last 5000 years. *Science Advances* **7**(26), eabe6102. doi: 10.1126/sciadv.abe6102

Cuffey KM and Paterson WSB (2010) *The Physics of Glaciers*, 4th Edn. Amsterdam: Academic Press, 704 pp.

Cuffey KM, Thorsteinsson T and Waddington ED (2000) A renewed argument for crystal size control of ice sheet strain rates. *Journal of Geophysical Research: Solid Earth* **105**(B12), 27889–27894. doi: 10.1029/2000JB900270

Dahl-Jensen D (1989) Steady thermomechanical flow along two-dimensional flow lines in large grounded ice sheets. *Journal of Geophysical Research: Solid Earth* **94**(B8), 10355–10362. doi: 10.1029/JB094iB08p10355

Dahl-Jensen D and Gundestrup NS (1987) Constitutive properties of ice at Dye 3, Greenland. In Waddinton ED and Walder J (eds), *The Physical Basis of Ice Sheet Modelling*, Proc Vancouver Symp, August 1987, (International Association of Hydrological Sciences Publication 170, Washington, DC), pp. 31–43.

Dansgaard W (1973) Stable isotope glaciology, Med. om Gr~bn.Bd. 197, No. 2, Reitzels Press, Copenhagen.

Durand G and 8 others (2009) Evolution of the texture along the EPICA Dome C Ice Core. *Low Temperature Science* **68**, 91–105.

Duval P and Lorius C (1980) Crystal size and climatic record down to the last ice age from Antarctic ice. *Earth and Planetary Science Letters* **48**(1), 59–64. doi: 10.1016/0012-821X(80)90170-3

Dyurgerov MB and Meier MF (2000) Twentieth century climate change: evidence from small glaciers. *Proceedings of the National Academy of Sciences* **97**(4), 1406–1411. doi: 10.1073/pnas.97.4.1406

El Kenawy A, López-Moreno JI and Vicente-Serrano SM (2012) Trend and variability of surface air temperature in northeastern Spain (1920–2006): linkage to atmospheric circulation. *Atmospheric Research* **106**, 159–180. doi: 10.1016/j.atmosres.2011.12.006

Engelbrecht JP and 5 others (2016) Technical note: mineralogical, chemical, morphological, and optical interrelationships of mineral dust re-suspensions. *Atmospheric Chemistry and Physics* **16**(17), 10809–10830. doi: 10.5194/acp-16-10809-2016

EPICA community members (2004) Eight glacial cycles from an Antarctic ice core. *Nature* **429**(6992), 623–628. doi: 10.1038/nature02599

Etheridge DM (1989) Dynamics of the Law Dome ice cap, Antarctica, as found from bore-hole measurements. *Annals of Glaciology* **12**, 46–50. doi: 10.3189/S0260305500006947

Faria SH and 6 others (2009) The multiscale structure of Antarctica. Part I: inland ice. *Low Temperature Science* **68**(suppl), 39–59.

Faria SH, Freitag J and Kipfstuhl S (2010) Polar ice structure and the integrity of ice-core paleoclimate records. *Quaternary Science Reviews* **29**(1–2), 338–351. doi: 10.1016/j.quascirev.2009.10.016

Faria SH, Hamann I, Kipfstuhl S and Miller H (2006) Is Antarctica like a birthday cake? Max Planck Institute for Mathematics in the Sciences, Leipzig, Germany. Communication preprint no. 33/06.

Faria SH, Kipfstuhl S and Lambrecht A (2018) *The EPICA-DML Deep Ice Core: A Visual Stratigraphy Record*. Heidelberg: Springer. https://www.springer.com/gp/book/9783662553060

Faria SH, Weikusat I and Azuma N (2014) The microstructure of polar ice. Part I: highlights from ice core research. *Journal of Structural Geology* **61**, 2–20. doi: 10.1016/j.jsg.2013.09.010

Fisher DA and Koerner RM (1986) On the special rheological properties of ancient microparticle-laden northern hemisphere ice as derived from bore-hole and core measurements. *Journal of Glaciology* **32**(112), 501–510. doi: 10.3189/S0022143000012211

Fitzpatrick JJ and 12 others (2014) Physical properties of the WAIS Divide ice core. *Journal of Glaciology* **60**(224), 1181–1198. doi: 10.3189/2014JoG14J100

Formenti P and 6 others (2014) Mapping the physico-chemical properties of mineral dust in western Africa: mineralogical composition. *Atmospheric Chemistry and Physics* **14**(19), 10663–10686. doi: 10.5194/acp-14-10663-2014

García Ruiz JM and Martí Bono CE (2002) Mapa geomorfológico del Parque Nacional de Ordesa y Monte Perdido. Organismo Autónomo de Parques Nacionales, Madrid, 106 pp., 2002.

Glen JW (1952) Experiments on the deformation of ice. *Journal of Glaciology* **2**(12), 111–114. doi: 10.3189/S0022143000034067

Glen JW (1955) The creep of polycrystalline ice. *Proceedings of the Royal Society of London. Series A* **228**, 519–538. doi: doi: 10.1098/rspa.1955.0066

Glen JW (1956) Measurement of the deformation of ice in a tunnel at the foot of an ice fall. *Journal of Glaciology* **2**(20), 735–746. doi: 10.3189/S0022143000025004

Goldsby DL and Kohlstedt DL (1997) Grain boundary sliding in fine-grained ice I. *Scripta Materialia* **37**(9), 1399–1406. doi: 10.1016/S1359-6462(97)00246-7

Goldsby DL and Kohlstedt DL (2001) Superplastic deformation of ice: experimental observations. *Journal of Geophysical Research: Solid Earth* **106**(B6), 11017–11030. doi: 10.1029/2000JB900336

Gow AJ (1968) Bubbles and bubble pressures in Antarctic glacier ice. *Journal of Glaciology* **7**(50), 167–182. doi: 10.3189/S0022143000030975

Gow AJ and Williamson T (1976). Rheological implications of the internal structure and crystal fabrics of the West Antarctic ice sheet as revealed by deep core drilling at Byrd Station. *Geological Society of America Bulletin* **87**(12), 1665. https://doi.org/10.1130/0016-7606(1976)87<1665:RIOTIS>2.0.CO;2

Grunewald K and Scheithauer J (2010) Europe's southernmost glaciers: response and adaptation to climate change. *Journal of Glaciology* **56**(195), 129–142. doi: 10.3189/002214310791190947

Guillet G, Preunkert S, Ravanel L, Montagnat M and Friedrich R (2021) Investigation of a cold-based ice apron on a high-mountain permafrost rock wall using ice texture analysis and micro- 14 C dating: a case study of the Triangle du Tacul ice apron (Mont Blanc massif, France). *Journal of Glaciology* **67**(266), 1205–1212. doi: 10.1017/jog.2021.65

Gundestrup NS and Hansen BL (1984) Bore-hole survey at Dye 3, South Greenland. *Journal of Glaciology* **30**(106), 282–288. doi: 10.3189/S0022143000006109

Habiby F and Humphreys FJ (1994) The effect of particle stimulated nucleation on the recrystallization texture of an AlSi alloy. *Scripta Metallurgica et Materialia* **30**(6), 787–790. doi: 10.1016/0956-716X(94)90200-3

Hambrey MJ (1975) The origin of foliation in glaciers: evidence from some Norwegian examples. *Journal of Glaciology* **14**(70), 181–185. doi: 10.3189/S0022143000013496

Hambrey MJ (1976) Debris, bubble, and crystal fabric characteristics of foliated glacier ice, Charles Rabots Bre, Okstindan, Norway. *Arctic and Alpine Research* **8**(1), 49. doi: 10.2307/1550609

Hambrey MJ (1977) Foliation, minor folds and strain in glacier ice. *Tectonophysics* **39**(1–3), 397–416. doi: 10.1016/0040-1951(77)90106-8

Hambrey MJ (1994) *Glacial Environments*. London: UCL Press, 296 pp.

Hambrey MJ and Lawson W (2000) Structural styles and deformation fields in glaciers: a review. *Geological Society, London, Special Publications* **176**(1), 59–83. doi: 10.1144/GSL.SP.2000.176

Hambrey MJ and Milnes AG (1977) Structural geology of an Alpine glacier (Griesgletscher, Valais, Switzerland). *Eclogae Geologicae Helvetiae* **70**, 66–684.

Hambrey MJ, Milnes AG and Siegenthaler H (1980) Dynamics and structure of Griesgletscher, Switzerland. *Journal of Glaciology* **25**(92), 215–228. doi: 10.3189/S0022143000010455

Hellmann S and 8 others (2021) Crystallographic analysis of temperate ice on Rhonegletscher, Swiss Alps. *The Cryosphere* **15**(2), 677–694. doi: 10.5194/tc-15-677-2021

Hooke RL and Hudleston PJ (1978) Origin of foliation in glaciers. *Journal of Glaciology* **20**(83), 285–299. doi: 10.3189/S0022143000013848

Huang Y and Humphreys FJ (2000) Subgrain growth and low angle boundary mobility in aluminium crystals of orientation {110} ⟨001⟩ . *Acta Materialia* **48**(8), 2017–2030. doi: 10.1016/S1359-6454(99)00418-8

Hudleston PJ (1977) Progressive deformation and development of fabric across zones of shear in glacial ice. In Saxena SK, Bhattacharji S, Annersten H and Stephansson O (eds), *Energetics of Geological Processes*. Berlin, Heidelberg: Springer, pp. 121–150. doi: 10.1007/978-3-642-86574-9_7.

Hudleston PJ (2015) Structures and fabrics in glacial ice: a review. *Journal of Structural Geology* **81**, 1–27. doi: 10.1016/j.jsg.2015.09.003

Huidobro J, Aramendia J, Arana G and Madariaga JM (2021) Geochemical characterization of the NWA 11273 lunar meteorite using nondestructive analytical techniques: original, shocked, and alteration mineral phases. *ACS Earth and Space Chemistry* **5**(6), 1333–1342. doi: 10.1021/acsearthspacechem.0c00329

Humphreys FJ and Hatherly M (2004) *Recrystallization and Related Annealing Phenomena*, 2nd Edn. Pergamon: Elsevier Science Ltd.

IPCC (2013) Intergovernmental Panel on Climate Change: Working Group I Contribution to the IPCC Fifth Assessment Report Climate Change. The Physical Science Basis; IPCC Cambridge University Press: Cambridge, UK; New York, NY, USA, 2013; p. 1535.

IPCC (2021) Climate Change 2021: The physical science basis. Contribution of Working Group I to the Sixth Assessment Report of the Intergovernmental Panel on Climate Change. (Masson-Delmotte VP and 18 others (eds.)) Cambridge University Press, Cambridge, United Kingdom and New York, NY, USA. doi: 10.1017/9781009157896

Jacka TH and Maccagnan M (1984) Ice crystallographic and strain rate changes with strain in compression and extension. *Cold Regions Science and Technology* **8**(3), 269–286. doi: 10.1016/0165-232X(84)90058-2

Jouzel J and 20 others (2007) Orbital and millennial Antarctic climate variability over the past 800,000 years. *Science* **317**(5839), 793–796. doi: 10.1126/science.1141038

Julián A and Chueca J (2007) Pérdidas de extensión y volumen en los glaciares del macizo de Monte Perdido (Pirineo central español): 1981–1999. *Boletín Glaciológico Aragonés* **8**, 31–60.

Kamb WB (1959) Ice petrofabric observations from Blue Glacier, Washington, in relation to theory and experiment. *Journal of Geophysical Research* **64**(11), 1891–1909. doi: 10.1029/JZ064i011p01891

Kawashima K and Yamada T (1997) Experimental studies on the transformation from firn to ice in the wet-snow zone of temperate glaciers. *Annals of Glaciology* **24**, 181–185. doi: 10.3189/S0260305500012143

Kerch J (2016) Crystal-orientation fabric variations on the cm-scale in cold Alpine ice: interaction with paleo-climate proxies under deformation and implications for the interpretation of seismic velocities (PhD thesis). Universität Heidelberg. doi: 10013/epic.49379.d001

Kipfstuhl S and 7 others (2006) Microstructure mapping: a new method for imaging deformation-induced microstructural features of ice on the grain scale. *Journal of Glaciology* **52**(178), 398–406. doi: 10.3189/172756506781828647

Kostecka JM and Whillans IM (1988) Mass balance along two transects of the west side of the Greenland ice sheet. *Journal of Glaciology* **34**(116), 31–39. doi: 10.3189/S0022143000009035

Langway CC (1958) Ice fabrics and the universal stage, US Army snow ice and permafrost research establishment, Tech. Rep. 62.

Lewis WV (ed.) (1960) *Norwegian Cirque Glaciers*, Vol. 4. London: Royal Geographical Society Research Series, 104 pp.

Li Z, Wang L, Chen H and Ma Q (2020) Degradation of emerald green: scientific studies on multi-polychrome Vairocana Statue in Dazu Rock Carvings, Chongqing, China. *Heritage Science* **8**(1), 64. doi: 10.1186/s40494-020-00410-2

Lipenkov VY, Barkov NI, Duval P and Pimienta P (1989) Crystalline texture of the 2083 m ice core at Vostok Station, Antarctica. *Journal of Glaciology* **35**(121), 392–398. doi: 10.3189/S0022143000009321

López-Moreno JI (2005) Recent variations of snowpack depth in the Central Spanish Pyrenees. *Arctic, Antarctic, and Alpine Research* **37**(2), 253–260. doi: 10.1657/1523-0430(2005)037[0253:RVOSDI]2.0.CO;2

López-Moreno JI and 10 others (2016) Thinning of the Monte Perdido Glacier in the Spanish Pyrenees since 1981. *The Cryosphere* **10**(2), 681–694. doi: 10.5194/tc-10-681-2016

López-Moreno JI and 14 others (2019) Ground-based remote-sensing techniques for diagnosis of the current state and recent evolution of the Monte Perdido Glacier, Spanish Pyrenees. *Journal of Glaciology* **65**(249), 85–100. doi: 10.1017/jog.2018.96

López-Moreno JI, Goyette S and Beniston M (2009) Impact of climate change on snowpack in the Pyrenees: horizontal spatial variability and vertical gradients. *Journal of Hydrology* **374**(3–4), 384–396. doi: 10.1016/j.jhydrol.2009.06.049

López-Moreno JI, Vicente-Serrano SM, Angulo-Martínez M, Beguería S and Kenawy A (2010) Trends in daily precipitation on the northeastern Iberian Peninsula, 1955-2006: trends in daily precipitation on the Iberian Peninsula. *International Journal of Climatology* **30**(7), 1026–1041. doi: 10.1002/joc.1945

Marcaida I and 7 others (2019) Raman microscopy as a tool to discriminate mineral phases of volcanic origin and contaminations on red and yellow ochre raw pigments from Pompeii. *Journal of Raman Spectroscopy*, **50**(2), 143–149. doi: 10.1002/jrs.5414

Marshall S (2014) Glacier retreat crosses a line. *Science* **345**(6199), 872–872. doi: 10.1126/science.1258584

Meier MF (1960) *Mode of Flow of Saskatchewan Glacier*, vol. **351**. Alberta, Canada. U.S. Geological Survey Professional Paper. 70 pp.

Meier MF, Rigsby GP and Sharp RP (1954) Preliminary data from Saskatchewan Glacier, Alberta, Canada. *ARCTIC* **7**(1), 3–26. doi: 10.14430/arctic3824

Miyamoto A and 10 others (1999) Ice-sheet flow conditions deduced from mechanical tests of ice core. *Annals of Glaciology* **29**, 179–183. doi: 10.3189/172756499781820950

Montagnat M and 10 others (2014) Fabric along the NEEM ice core, Greenland, and its comparison with GRIP and NGRIP ice cores. *The Cryosphere* **8**(4), 1129–1138. doi: 10.5194/tc-8-1129-2014

Monz ME and 8 others (2021) Full crystallographic orientation (c and a axes) of warm, coarse-grained ice in a shear-dominated setting: a case study, Storglaciären, Sweden. *The Cryosphere* **15**(1), 303–324. doi: 10.5194/tc-15-303-2021

Moreno A and 24 others (2021) The case of a southern European glacier which survived Roman and medieval warm periods but is disappearing under recent warming. *The Cryosphere* **15**(2), 1157–1172. doi: 10.5194/tc-15-1157-2021

Mullins WW (1957) Theory of thermal grooving. *Journal of Applied Physics* **28**(3), 333–339. doi: 10.1063/1.1722742

Nishida K and Narita H (1996) Three-dimensional observations of ice crystal characteristics in polar ice sheets. *Journal of Geophysical Research: Atmospheres* **101**(D16), 21311–21317. doi: 10.1029/96JD01770

Paterson WSB (1991) Why ice-age ice is sometimes 'soft'. *Cold Regions Science and Technology* **20**(1), 75–98. doi: 10.1016/0165-232X(91)90058-O

Paterson WSB (1994) *The Physics of Glaciers*, 3rd Edn. Oxford, UK: Elsevier Science Ltd, 481 pp.

Pérez-Zanón N, Sigró J and Ashcroft L (2017) Temperature and precipitation regional climate series over the central Pyrenees during 1910–2013: regional climate series over the central Pyrenees during 1910-2013. *International Journal of Climatology* **37**(4), 1922–1937. doi: 10.1002/joc.4823

Perutz MF and Seligman G (1939) A crystallographic investigation of glacier structure and the mechanism of glacier flow. *Proceedings of the Royal Society of London. Series A. Mathematical and Physical Sciences* **172**(950), 335–360. doi: 10.1098/rspa.1939.0108

Petit JR, Duval P and Lorius C (1987) Long-term climatic changes indicated by crystal growth in polar ice. *Nature* **326**(6108), 62–64. doi: 10.1038/326062a0

Pey J and 8 others (2020) Snow impurities in the central Pyrenees: from their geochemical and mineralogical composition towards their impacts on snow albedo. *Atmosphere* **11**(9), 937. doi: 10.3390/atmos11090937

Pey J, Querol X, Alastuey A, Forastiere F and Stafoggia M (2013) African dust outbreaks over the Mediterranean Basin during 2001–2011: PM10 concentrations, phenomenology and trends, and its relation with synoptic and mesoscale meteorology. *Atmospheric Chemistry and Physics* **13**(3), 1395–1410. doi: 10.5194/acp-13-1395-2013

Pfeffer WT (1992) Stress-induced foliation in the terminus of Variegated Glacier, Alaska, USA, formed during the 1982–83 surge. *Journal of Glaciology* **38**, 213–222.

Prospero JM, Ginoux P, Torres O, Nicholson SE and Gill TE (2002) Environmental characterization of global sources of atmospheric soil dust identified with the nimbus 7 total ozone mapping spectrometer (toms) absorbing aerosol product: global sources of atmospheric soil dust. *Reviews of Geophysics* **40**(1), 2-1–2-31. doi: 10.1029/2000RG000095

Ragan DM (1969) Structures at the base of an ice fall. *The Journal of Geology* **77**(6), 647–667. doi: 10.1086/627463

Reeh N (1988) A flow-line model for calculating the surface profile and the velocity, strain-rate, and stress fields in an ice sheet. *Journal of Glaciology* **34**(116), 46–55. doi: 10.3189/S0022143000009059

Rico I, Izagirre E, Serrano E and López-Moreno JI (2017) Superficie glaciar actual en los Pirineos: Una actualización para 2016. *Pirineos* **172**, 029. doi: 10.3989/Pirineos.2017.172004

Rigsby GP (1951) Crystal fabric studies on emmons Glacier Mount Rainier, Washington. *The Journal of Geology* **59**(6), 590–598. doi: 10.1086/625914

Rigsby GP (1953) *Studies of crystal fabrics and structures in glaciers: Pasadena* (Ph.D. dissertation). California, California Institute of Technology, 56 p.

Rigsby GP (1960) Crystal orientation in glacier and in experimentally deformed ice. *Journal of Glaciology* **3**(27), 589–606. doi: 10.3189/S0022143000023716

Robador Moreno A, Rodríguez Fernández R, Carcavilla Urquí L, Samsó Escolà JM and Martínez Rius A (2020) Parque Nacional de Ordesa y Monte Perdido: Guía geológica. *Instituto Geológico y Minero de España Organismo Autónomo Parques Nacionales*, 227 pp.

Saylor DM and Rohrer GS (1999) Measuring the influence of grain-boundary misorientation on thermal groove geometry in ceramic polycrystals. *Journal of the American Ceramic Society* **82**(6), 1529–1536. doi: 10.1111/j.1151-2916.1999.tb01951.x

Scheuvens D, Schütz L, Kandler K, Ebert M and Weinbruch S (2013) Bulk composition of northern African dust and its source sediments – a compilation. *Earth-Science Reviews* **116**, 170–194. doi: 10.1016/j.earscirev.2012.08.005

Schwarzacher W and Untersteiner N (1953) Zum problem der bänderung des gletschereises. sitzungsberichten der österreichischen akademie der wissenschaften. Mathematisch-Naturwissenschaftliche Klasse, Abt. 2A, Bd. 162, Ht. 1–4, pp. 111–145.

Schytt V (1955) Glaciological investigations in the Thulc Ramp area. US. Snow, Ice and Permafrost Research Establishment. Report 28.

Shoji H and Langway CC (1987) Flow velocity profiles and accumulation rates from mechanical tests on ice core samples. IUGG General Assembly of Vancouver, Aug. 1987, IAHS Publ., 170: 67-77.

Shumskii PA (1964) *Principles of Structural Glaciology.* (Translated from the Russian by Kraus, D.). New York: Dover Publications.

Somerday M and Humphreys FJ (2003) Recrystallisation behaviour of supersaturated Al–Mn alloys Part 1 – Al–1.3 wt-%Mn. *Materials Science and Technology* **19**(1), 20–29. doi: 10.1179/026708303225008590

Song M, Baker I and Cole DM (2005) The effect of particles on dynamic recrystallization and fabric development of granular ice during creep. *Journal of Glaciology* **51**(174), 377–382. doi: 10.3189/172756505781829287

Sousa PM and 5 others (2019) Saharan air intrusions as a relevant mechanism for Iberian heatwaves: the record breaking events of August 2018 and June 2019. *Weather and Climate Extremes* **26**, 100224. doi: 10.1016/j.wace.2019.100224

Swinzow GK (1962) Investigation of shear zones in the ice sheet margin, Thule Area, Greenland. *Journal of Glaciology* **4**(32), 215–229. doi: 10.3189/S0022143000027416

Thomas N and Nigam S (2018) Twentieth-century climate change over Africa: seasonal hydroclimate trends and Sahara desert expansion. *Journal of Climate* **31**(9), 3349–3370. doi: 10.1175/JCLI-D-17-0187.1

Thorsteinsson T, Kipfstuhl J, Eicken H, Johnsen SJ and Fuhrer K (1995) Crystal size variations in Eemian-age ice from the GRIP ice core, Central Greenland. *Earth and Planetary Science Letters* **131**(3–4), 381–394. doi: 10.1016/0012-821X(95)00031-7

Thorsteinsson T, Kipfstuhl J and Miller H (1997) Textures and fabrics in the GRIP ice core. *Journal of Geophysical Research: Oceans* **102**(C12), 26583–26599. doi: 10.1029/97JC00161

Tison JL and Hubbard B (2000) Ice crystallographic evolution at a temperate glacier: Glacier de Tsanfleuron, Switzerland. *Geological Society, London, Special Publications* **176**(1), 23–38. doi: 10.1144/GSL.SP.2000.176.01.03

Treverrow A, Budd WF, Jacka TH and Warner RC (2012) The tertiary creep of polycrystalline ice: experimental evidence for stress-dependent levels of strain-rate enhancement. *Journal of Glaciology* **58**(208), 301–314. doi: doi: 10.3189/2012JoG11J149

Vidaller I and 12 others (2021) Toward an ice-free mountain range: demise of Pyrenean glaciers during 2011–2020. *Geophysical Research Letters* **48**(18). doi: 10.1029/2021GL094339

Wadham JL and Nuttall AM (2002) Multiphase formation of superimposed ice during a mass-balance year at a maritime high-Arctic glacier. *Journal of Glaciology* **48**(163), 545–551. doi: 10.3189/172756502781831025

Weertman J and Weertman JR (1992) *Elementary Dislocation Theory.* Oxford: Oxford University Press.

Weikusat I and 10 others (2017) Physical analysis of an Antarctic ice core – towards an integration of micro- and macrodynamics of polar ice. *Philosophical Transactions of the Royal Society A: Mathematical, Physical and Engineering Sciences* **375**(2086), 20150347. doi: 10.1098/rsta.2015.0347

Zhang Q, Kang S, Gabrielli P, Loewen M and Schwikowski M (2015) Vanishing high mountain glacial archives: challenges and perspectives. *Environmental Science & Technology* **49**(16), 9499–9500. doi: 10.1021/acs.est.5b03066

https://doi.org/10.1017/aog.2023.66 Published online by Cambridge University Press